remote sensing

MDPI

Article

Mapping Soil Moisture at a High Resolution over Mountainous Regions by Integrating In Situ Measurements, Topography Data, and MODIS Land Surface Temperatures

Lei Fan [1,2,*], A. Al-Yaari [2], Frédéric Frappart [3,4], Jennifer J. Swenson [5], Qing Xiao [6,7], Jianguang Wen [6,7], Rui Jin [8], Jian Kang [8], Xiaojun Li [2], R. Fernandez-Moran [9] and J.-P. Wigneron [2,*]

1 Collaborative Innovation Center on Forecast and Evaluation of Meteorological Disaster, School of Geographical Sciences, Nanjing University of Information Science and Technology, Nanjing 210044, China
2 UMR 1391 ISPA, INRA, F-33140 Villenave d'Ornon, France; amen.al-yaari@inra.fr (A.A.-Y.); Xiaojun.Li@inra.fr (X.L.)
3 Laboratoire d'Etudes en Géophysique et Océanographie Spatiales (LEGOS), 31400 Toulouse, French; frederic.frappart@gmail.com
4 Géosciences Environnement Toulouse (GET), 31400 Toulouse, France
5 Nicholas School of the Environment, Duke University, Durham, NC 27708, USA; jswenson@duke.edu
6 State Key Laboratory of Remote Sensing Science, Institute of Remote Sensing and Digital Earth, Chinese Academy of Sciences, Beijing 100101, China; xiaoqing@radi.ac.cn (Q.X.); wenjg@radi.ac.cn (J.W.)
7 University of Chinese Academy of Sciences, Beijing 100049, China
8 Key Laboratory of Remote Sensing of Gansu Province, Heihe Remote Sensing Experimental Research Station, Northwest Institute of Eco-Environment and Resources, Chinese Academy of Sciences, Lanzhou 730000, China; jinrui@lzb.ac.cn (R.J.); kangjian@lzb.ac.cn (J.K.)
9 Image Processing Laboratory (IPL), University of Valencia, 91354 Valencia, Spain; roberto.fernandez@uv.es
* Correspondence: lei.fan@inra.fr (L.F.); jean-pierre.wigneron@inra.fr (J.-P.W.)

Received: 30 January 2019; Accepted: 14 March 2019; Published: 18 March 2019

Abstract: Hydro-agricultural applications often require surface soil moisture (SM) information at high spatial resolutions. In this study, daily spatial patterns of SM at a spatial resolution of 1 km over the Babao River Basin in northwestern China were mapped using a Bayesian-based upscaling algorithm, which upscaled point-scale measurements to the grid-scale (1 km) by retrieving SM information using Moderate Resolution Imaging Spectroradiometer (MODIS)-derived land surface temperature (LST) and topography data (including aspect and elevation data) and in situ measurements from a wireless sensor network (WSN). First, the time series of pixel-scale (1 km) representative SM information was retrieved from in situ measurements of SM, topography data, and LST. Second, Bayesian linear regression was used to calibrate the relationship between the representative SM and the WSN measurements. Last, the calibrated relationship was used to upscale a network of in situ measured SM to map spatially continuous SM at a high resolution. The upscaled SM data were evaluated against ground-based SM measurements with satisfactory accuracy—the overall correlation coefficient (r), slope, and unbiased root mean square difference (ubRMSD) values were 0.82, 0.61, and 0.025 m^3/m^3, respectively. Moreover, when accounting for topography, the proposed upscaling algorithm outperformed the algorithm based only on SM derived from LST (r = 0.80, slope = 0.31, and ubRMSD = 0.033 m^3/m^3). Notably, the proposed upscaling algorithm was able to capture the dynamics of SM under extreme dry and wet conditions. In conclusion, the proposed upscaled method can provide accurate high-resolution SM estimates for hydro-agricultural applications.

Keywords: upscaling; soil moisture; high resolution; Bayesian linear regression; wireless sensor network; topographic effects

1. Introduction

Soil moisture (SM) is a critical hydrological variable that links terrestrial water, energy, and carbon cycles [1–3]. Most hydro-agricultural applications rely on SM measurements at fine spatial resolutions (~1 km) with continuous temporal coverage [4,5]. However, current satellite missions provide regional-scale SM observations at coarse spatial resolutions (lower than 25 km) [6–8].

Various approaches for estimating high-resolution SM have been proposed by downscaling coarse passive microwave data with fine-scale auxiliary variables. The Soil Moisture Active Passive (SMAP) mission was designed to combine high-resolution active and coarse passive microwave measurements at L-band in order to provide SM data at 9 km resolution [9]. Other downscaling algorithms were proposed based on a combination of coarse resolution passive microwave data (e.g., Soil Moisture and Ocean Salinity (SMOS) and Advanced Microwave Scanning Radiometer for EOS (AMSR-E)) with moderate resolution optical/thermal sensors data (e.g., the Moderate Resolution Imaging Spectroradiometer (MODIS)) [4,10–12], which have better temporal resolution than operational radar sensors. However, uncertainties in passive microwave SM products would degrade the accuracy of the downscaled SM [13]. Especially over mountainous regions, topographic effects further increase the uncertainties in the optimization of some parameters (e.g., vegetation properties and surface roughness) required to retrieve passive microwave SM products [14].

On the other hand, the point-scale in situ SM measurements can be extrapolated to larger scales to obtain high-resolution SM estimates via geostatistical techniques [15,16]. However, these point measurements are not representative of the neighboring areas because of the large spatial heterogeneity of SM over a range of scales. With the development of the wireless sensor networks (WSNs) [17,18], several upscaling strategies, such as machine learning [19], kriging [20], and the Bayesian maximum entropy (BME) method [21,22], have been proposed to estimate high resolution SM by merging WSNs and optical/thermal remote sensing data [23]. The idea behind these upscaling methods is to aggregate SM observations from multi-point WSN measurements at the remote-sensing pixel level with the help of vegetation cover and surface temperature information, as well as other surface parameters obtained from optical and/or thermal sensors [23]. A range of optical SM indicators has successfully been merged with WSNs to obtain high-resolution SM, such as land surface temperature (LST) [20], temperature vegetation dryness index (TVDI) [22,24], soil evaporative efficiency (SEE) [22], and apparent thermal inertia (ATI) [25]. However, these methods are only applicable under clear-sky conditions because of the effects of cloud coverage on optical data, which limits monitoring of SM temporal dynamics, albeit with high spatial resolution. This restriction is critical because assessing the temporal dynamics of SM is needed for regional-scale applications, such as agriculture for irrigation scheduling and site-specific management against diseases and pests [26].

The Bayesian linear regression (BLR) upscaling algorithm [27] has the potential to both address the issue of temporal discontinuity in high-resolution SM products and improve the SM estimates [25,28]. The BLR upscaling algorithm is composed of two steps: i) the calibration of the relationship between the time-series in situ SM observations and the pixel-scale SM retrieved by optical/thermal time-series information; ii) the use of this relationship to upscale the in situ observations to obtain a continuous time-series of high-resolution (~1 km) SM observations [28]. However, the relationships between the in situ observations and the upscaled SM could be non-robust because of missing optical/thermal observations under non-clear-sky conditions. The non-robustness of the relationship can be attributed to the fact that most available optical/thermal observations are obtained during the drier times of year, leading to bias in the calibrated relationship towards low SM values. Additionally, the application of the BLR upscaling algorithm is limited over mountainous areas because of topographic effects,

which could mask the SM information retrieved from optical/thermal indices (e.g., TVDI and ATI) [29]. For example, ATI is derived from LST and albedo, but topography has a large influence on albedo retrievals, with values that can change up to 100% for the same land-cover class under varying slopes and aspect of the terrain [30]. Consequently, uncertainties in both the optical/thermal observations and the BLR approach could lead to biased SM estimates. Therefore, additional information is required to limit the uncertainties in the BLR estimates.

The Babao River basin, as a sub-basin in the upper reaches of the Heihe River Basin (HRB), produces water resource for agriculture in the middle reach and the downstream region of the HRB [18]. Scarcity of water resources has significantly restricted social and economic developments in this area [31]. Thus, high-resolution SM information is an urgent need for the ecological environmental management in the Babao River basin [18]. Previous studies [25] attempted to map SM at high resolution over this area, but the complex topography conditions and missing observations due to non-clear-sky conditions in the Babao River basin were not adequately considered, as mentioned above.

Here, we propose an upscaling approach to retrieve daily SM with a spatial resolution of 1 km in the Babao River basin, using the BLR method to upscale WSN multi-point observations considering topographic complexity. This was achieved using remote sensing information (e.g., ASTER aspect and elevation and MODIS LST). The WSN measurements, MODIS LST, and topography data are presented in Section 2; the upscaling approach and the statistical metrics used to evaluate the upscaled SM are explained in Section 3; and results are given in Section 4. Section 5 discusses the findings and the main conclusions are drawn in Section 6.

2. Study Area and Datasets

2.1. Study Area

The Babao River Basin (covering 2495 km^2, Figure 1a) is located in the eastern branch of the upper reach of the Heihe River Basin, which is also the main study area for hydrological research in the cold region of the Heihe Watershed Allied Telemetry Experimental Research (HiWATER) project [18]. The Babao River Basin is mainly covered with grasslands (Figure 1b), with elevation ranging from 2640 to 5000 m, with an average of 3604 m. The rainy season spans from May to September. The heterogeneous distributions of both rainfall and topography (e.g., shady/sunny slopes) strongly influence the spatial and temporal variability of SM [32]. The Babao River Basin is a cloudy area, and the cloudy period generally exceeds half the year as a result of a combination of westerlies, East Asia monsoon, and Tibetan Plateau monsoon [33]. The study period was from 1 July 2015 to 15 October 2015 and avoided snow periods.

2.2. In Situ Measurements

A wireless sensor network, the Ecological and Hydrological Wireless Sensor Network (EHWSN), was established to measure SM and soil temperature at depths of 4, 10, and 20 cm at 5 min intervals in the Babao River Basin [34]. EHWSN is composed of 37 ground-based sites installed in 2012 to monitor the SM dynamics [32], but parts of sites were offline because of equipment failure. In 2015, there were 16 WSN sites providing SM observations over the study periods (Figure 1a and Table 1). Additionally, the 4 cm SM observations from the A'rou superstation and the A'rou sunny automatic meteorological stations (AMSs) are also used in the study (Figure 1a and Table 1) [35].

2.3. Remote Sensing Products

MODIS Terra LST product (MOD11A1), which provides both day-time and night-time daily LST at 1 km spatial resolution [36], was used to retrieve SM. Data acquired during the period from 1 July 2015 to 15 October 2015 were used in this study, avoiding snow periods as snow cover results in uncertainties in LST products [37].

The elevation (Figure 1a) and aspect (Figure 1c) data were derived from the Advanced Spaceborne Thermal Emission and Reflectance Radiometer (ASTER) Global Digital Elevation Model (GDEM) version 2 product [38]. A simple average method was applied to aggregate the 30 m resolution data into 1 km resolution data to match the grids of MODIS LST products.

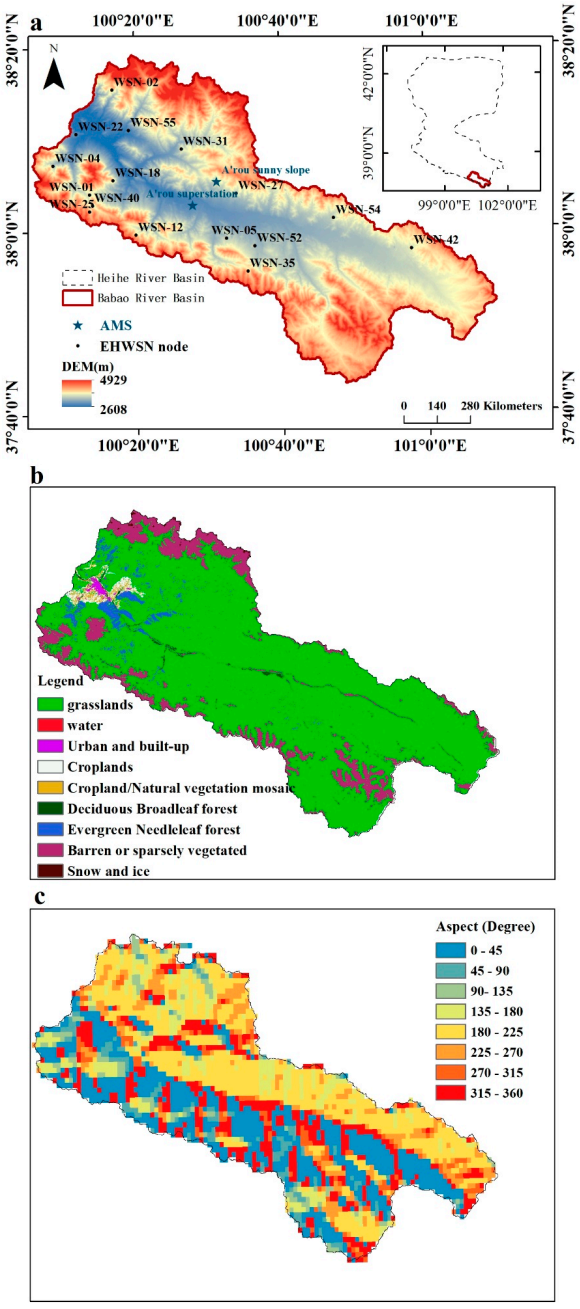

Figure 1. Study area and spatial distributions of ground-based stations (**a**), land cover types (**b**), and aspect (**c**). (**a**) The wireless sensor network (WSN) sites are marked as black points and the automatic meteorological station (AMS) sites are represented by blue stars. Elevation information is also presented based on a digital elevation model (DEM) with a spatial resolution of 30 m shared freely by Advanced Spaceborne Thermal Emission and Reflectance Radiometer (ASTER) Global Digital Elevation Model (GDEM). (**b**) Land cover types data at a spatial resolution of 30 m provide by the Heihe Watershed Allied Telemetry Experimental Research (HiWATER) project [39]. (**c**) Terrain aspect data retrieved using 1 km GDEM, which was aggregated from 30 m GDEM data. EHWSN—Ecological and Hydrological Wireless Sensor Network.

Table 1. Observation periods, depth, and temporal resolution of the wireless sensor network (WSN) and automatic meteorological station (AMS) nodes. Site locations and elevations of each node were listed in Kang et al. (2017) [25]. EHWSN—Ecological and Hydrological Wireless Sensor Network.

Station	Type	Observation Period during 2015	Observation Depth	Temporal Resolution
WSN-01	EHWSN	1 January to 25 August	4, 10, 20 cm	5 min
WSN-02	EHWSN	1 January to 23 October	4, 10, 20 cm	5 min
WSN-04	EHWSN	1 January to 31 December	4, 10, 20 cm	5 min
WSN-05	EHWSN	1 January to 31 December	4, 10, 20 cm	5 min
WSN-12	EHWSN	13 March to 31 December	4, 10, 20 cm	5 min
WSN-18	EHWSN	1 January to 31 December	4, 10, 20 cm	5 min
WSN-22	EHWSN	1 January to 31 December	4, 10, 20 cm	5 min
WSN-25	EHWSN	1 January to 31 December	4, 10, 20 cm	5 min
WSN-27	EHWSN	6 August to 31 December	4, 10, 20 cm	5 min
WSN-31	EHWSN	1 January to 31 December	4, 10, 20 cm	5 min
WSN-35	EHWSN	1 January to 31 December	4, 10, 20 cm	5 min
WSN-40	EHWSN	1 January to 29 October	4, 10, 20 cm	5 min
WSN-42	EHWSN	1 January to 31 December	4, 10, 20 cm	5 min
WSN-52	EHWSN	30 January to 31 December	4, 10, 20 cm	5 min
WSN-54	EHWSN	1 January to 31 December	4, 10, 20 cm	5 min
WSN-55	EHWSN	1 January to 31 December	4, 10, 20 cm	5 min
A'rou superstation	AMS	1 January to 31 December	2, 4, 6, 10, 15, 20, 30, 40, 60, 80, 120, 160, 200, 240, 280, 320 cm	10 min
A'rou sunny slope	AMS	1 January to 9 September	4, 10, 20, 40, 80, 120, 160 cm	10 min

3. Methods

3.1. The Bayesian Linear Regression (BLR) Upscaling Algorithm

The strategy used to spatially upscale the WSN measurements was previously proposed by Qin et al. (2013) [28], and was used over the Babao River Basin by Kang et al. (2017) [25]. The theoretical formulation assumes that the transformation function between the WSN measured SM (θ^{WSN}) and the upscaled SM ($\theta^{upscale}$) is linear; $\theta^{upscale}$ at a grid (1 km) from time t_1 to t_M can be calculated as follows:

$$\theta^{upscale} = W^T D^{WSN} \text{ and } D^{WSN} = \left[1,\ \theta^{WSN}\right]^T, \tag{1}$$

where $\theta^{upscale}$ is a column vector $\left[\theta_{t1}^{upscale}, \theta_{t2}^{upscale}, \ldots,\ \theta_{tM}^{upscale}\right]$. W is the vector of the combination coefficients $[W_0, W_1, \ldots,\ W_N]^T$. W_0 is a constant term and W_N is the weighted coefficient of the Nth WSN observation node. D^{WSN} is the observation matrix of the θ^{WSN}, and θ^{WSN} is expressed as follows:

$$\begin{bmatrix} \theta_{t_1,\,1}^{WSN} & \cdots & \theta_{t_1,\,N}^{WSN} \\ \vdots & \ddots & \vdots \\ \theta_{t_M,\,1}^{WSN} & \cdots & \theta_{t_M,\,N}^{WSN} \end{bmatrix}, \tag{2}$$

where $\theta_{t_M,\,N}^{WSN}$ represents the SM measurement from the Nth WSN node at time t_M and M is the number of time series observations.

To calculate W at a grid point, a cost function is established in Equation (3) by combining D^{WSN} and $\theta^{upscale}$ at the grid point.

$$J = \left(D^{WSN}W - \theta^{upscale}\right)^T \left(D^{WSN}W - \theta^{upscale}\right). \tag{3}$$

W can be derived using the ordinary least-squares (OLS) method by minimizing the cost function. In practice, $\theta^{upscale}$, as an estimated variable, cannot be obtained, but $\theta^{upscale}$ can be replaced by

a representative SM (θ^{rep}) with random noise [28], as shown in Equation (4). The calculation of θ^{rep} was described in Section 3.2.

$$J = \left(D^{WSN}W - \theta^{rep}\right)^T \left(D^{WSN}W - \theta^{rep}\right) \quad (4)$$

In Equation (4), the accuracy of θ^{rep} is the key to the estimates of $\theta^{upscale}$, but θ^{rep} cannot accurately represent the dynamics in SM. The uncertainties in θ^{rep} could result in overfitting the value of W calculated using Equation (4). To reduce these overfitting effects, a regularization term is added to Equation (4), which can be re-written as follows [28]:

$$J = \left(D^{WSN}W - \theta^{rep}\right)^T \sigma^{-2} \left(D^{WSN}W - \theta^{rep}\right) + \alpha W^T W, \quad (5)$$

where σ is the standard deviation of θ^{rep}. α is the unknown regularization parameter, which can be estimated using the BLR approach based on the iteration strategy proposed by Chen et al. (2009) [27] and Qin et al. (2013) [28]. Finally, the upscaling coefficient W for each grid was calculated using Equation (5), after which it was used in Equation (1) to estimate $\theta^{upscale}$ at each grid. For more details about the BLR approach, please refer to Qin et al. (2013) [28] and Kang et al. (2017) [25].

3.2. Representative Soil Moisture

As mentioned above, the representative SM information (θ^{rep}) at grid-scale (1 km) was used to upscale multi-point WSN observations to map grid-scale SM. Kang et al. (2017) [25] used ATI-derived SM as θ^{rep} in the Babao River Basin. ATI can be computed as follows:

$$ATI = A\frac{1-\omega}{\Delta LST}, \quad (6)$$

where A is the solar correction factor and ω is the surface albedo. ΔLST denotes the maximum daily amplitude of LST and can be directly derived from the daily day/night MODIS LST products. However, over the study period, we found that there is no significant relationship between ATI and the in situ measured SM, but ΔLST is significantly related to the in situ measured SM. Uncertainties in the estimates of the surface albedo ω caused by the topographic effects could result in the failure of ATI to represent surface water status over the study region, as mentioned in the Introduction. Therefore, ΔLST is used to retrieve the representative SM ($\theta^{rep}_{\Delta \mathrm{LST}}$) using a linear regression relationship as follows:

$$\theta^{rep}_{\Delta LST} = a\Delta LST + b. \quad (7)$$

Note that over the study period, the availability of ΔLST is severely affected by clouds, resulting in a high rate (88.6%) of missing ΔLST data (Figure 2). The serious lack of availability of $\theta^{rep}_{\Delta LST}$ will increase the uncertainties in the BLR upscaling algorithm; thus, additional SM information should be introduced into the upscaling process.

The topographic factors (e.g., shady/sunny slopes and elevation), as the main factors controlling the heterogeneous distributions of SM over the mountainous regions, have the potential to provide additional SM information to overcome the serious lack of availability of $\theta^{rep}_{\Delta LST}$. Over the mountainous regions, the strong variability of both temperature and precipitation associated with elevation and terrain aspect has an important impact on the SM patterns. Here, elevation and terrain aspect were combined with the in situ measured SM to derive the representative SM (θ^{rep}_{topo}). This latter variable is then combined with $\theta^{rep}_{\Delta LST}$ to construct the continuous time-series of representative SM ($\theta^{rep}_{topo,\ \Delta \mathrm{LST}}$). The different steps of the retrieval of $\theta^{rep}_{topo,\ \Delta \mathrm{LST}}$ are detailed below:

(a) Retrieval of $\theta^{rep}_{\mathrm{topo}}$

The study region was split into four sub-regions using the elevation (Figure 1a) and aspect (Figure 1c) data—the high-altitude with sunny slopes, the low-altitude with sunny slopes, the high-altitude with shady slopes, and the low-altitude with shady slopes regions. Accordingly, the representative SM ($\theta^{rep}_{t,\ topo}$) at the date t over the study region can be constructed by the averaged SM over each sub-region, which can be represented by $\theta_t^{high-altitude,\ sunny}$, $\theta_t^{low-altitude,\ sunny}$, $\theta_t^{high-altitude,\ shady}$, and $\theta_t^{low-altitude,\ shady}$, respectively, expressed by Equation (8). The averaged SM value at the date t over each sub-region was calculated by averaging the SM values at the date t measured by the WSN nodes located in the corresponding sub-region. The WSN nodes located in each sub-region are listed in Table 1. The shady slopes (away from the sun, i.e., north aspect in the Northern Hemisphere) were defined as the aspects between 0 and 90° and between 270 and 360°, while sunny slopes facing towards the sun (i.e., south aspect) were defined as aspect between 90 and 270° (aspects calculated from ASTER GDEM data). High-altitude regions were considered to be >3600 m in elevation, while low-altitude regions were <3600 m.

$$\theta^{rep}_{t,\ topo} = \theta_t^{high-altitude,\ sunny} + \theta_t^{low-altitude,\ sunny} + \theta_t^{high-altitude,\ shady} + \theta_t^{low-altitude,\ shady} \quad (8)$$

(b) Retrieval of $\theta^{rep}_{topo,\ \Delta LST}$ by combining $\theta^{rep}_{\text{topo}}$ and $\theta^{rep}_{\Delta LST}$.

The time-series data of $\theta^{rep}_{\Delta LST}$ over the study region are able to capture the spatio-temporal variability of SM, but with large missing observations, while the continuous time-series data of $\theta^{rep}_{\text{topo}}$ have the capability to represent the temporally continuous dynamics of SM, but with low spatial details because $\theta^{rep}_{\text{topo}}$ was constructed from data over only four sub-regions. Thus, the time-series data of $\theta^{rep}_{topo,\ \Delta LST}$ were produced by combining $\theta^{rep}_{\Delta LST}$ and θ^{rep}_{topo}. To construct $\theta^{rep}_{t,\ topo,\ \Delta LST}$ on the date t, the missing pixels of $\theta^{rep}_{t,\ \Delta LST}$ on the date t were identified, then they were replaced by the SM values from the corresponding pixels of $\theta^{rep}_{t,\ topo}$. The combined $\theta^{rep}_{topo,\ \Delta LST}$ was a continuous time-series of SM estimates with a spatial resolution of 1 km. $\theta^{rep}_{topo,\ \Delta LST}$ was considered as the representative SM to be used in the BLR upscaling algorithm to produce high-resolution SM data.

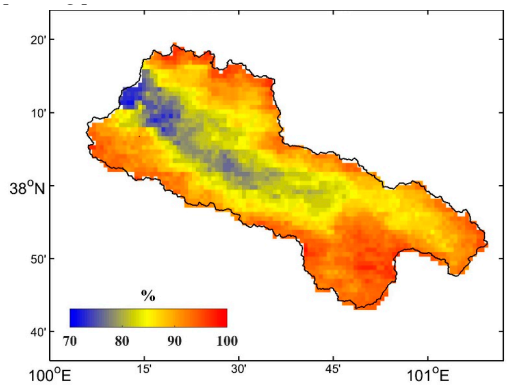

Figure 2. Spatial distribution of the missing Moderate Resolution Imaging Spectroradiometer (MODIS)-derived maximum daily amplitude of land surface temperature (LST) (ΔLST) data (1 km resolution) between 1 July 2015 and 15 October 2015.

3.3. Validation

Given that the number of available ground-measurements is not sufficient to separate them between training and validation datasets, 10-fold cross-validation methods [40–42] were used to evaluate the upscaled SM by comparing them against the in situ measurements from the sixteen WSN sites. In addition, the upscaled SM estimates were also evaluated by comparing them against the SM data measured by two AMSs. For more details about the cross-validation method, please refer to Cawley et al. (2003) [40].

3.4. Evaluation Metrics

The root mean square error (RMSE) is severely compromised if there are biases in either the mean or the amplitude of fluctuations in the estimates, thus we used a non-biased estimation of the error (unbiased-RMSE) where the mean bias is removed, as shown in Equation (9) [43]. Given that the distribution of SM within each 1 km grid is generally heterogeneous, and the ground measurements also include measurement uncertainties, the term 'error' was replaced by 'difference' in these metrics, that is, the root mean square difference (RMSD) and the unbiased root mean square difference (ubRMSD, m^3/m^3). Thus, ubRMSD is used to compare the upscaled SM product with the in situ measurements, which can be calculated using Equation (10) [43].

$$ubRMSD = \sqrt{(RMSD^2 - Bias^2)}, \tag{9}$$

$$ubRMSD = \sqrt{\frac{1}{N}\sum_{t=1}^{N}\left(\theta_t^{upscale} - \overline{\theta^{upscale}}\right)^2 - \left(\frac{1}{N}\sum_{t=1}^{N}\left(\theta_t^{In\ situ} - \overline{\theta^{In\ situ}}\right)\right)^2}, \tag{10}$$

where N is the number of the in situ observations (e.g., from WSN and AMS) in the time-series and $\theta_t^{In\ situ}$ are the in situ measurements from WSN and AMS on date t. $\overline{\theta^{In\ situ}}$ and $\overline{\theta^{upscale}}$ are the mean values of the corresponding time series.

In addition to the error evaluation, it is necessary to assess the consistency between datasets at each grid using *slope* values calculated using a linear regression relationship between $\theta^{upscale}$ and $\theta^{In\ situ}$ from Equation (11). The correlation coefficient r, calculated using Equation (12), is also used to assess the agreement between the estimates and the in situ measurements.

$$\theta^{In\ situ} = slope \cdot \theta^{upscale} + intercept \tag{11}$$

$$r = \frac{\sum_{t=1}^{N}\left(\theta_t^{upscale} - \overline{\theta^{upscale}}\right)\left(\theta_t^{WSN} - \overline{\theta^{in\ situ}}\right)}{\sqrt{\sum_{t=1}^{N}\left(\theta_t^{upscale} - \overline{\theta^{upscale}}\right)^2 \cdot \sum_{t=1}^{N}\left(\theta_t^{WSN} - \overline{\theta^{in\ situ}}\right)^2}} \tag{12}$$

4. Results

4.1. Representative Soil Moisture

MODIS-derived ΔLST was used to derive representative SM ($\theta_{\Delta LST}^{rep}$) by applying a regression analysis between the pixel-averaged ΔLST and the in situ measured SM from 16 WSN sites. It is difficult to construct a daily relationship model based on few available pairs of ΔLST and in situ measurements, because of the serious lack of observations in MODIS-derived ΔLST. We made full use of all matched pairs in the time-series to estimate the relationship between ΔLST and the in situ measurements. It can be observed from the scatter plot (Figure 3) between ΔLST and the in situ measurements that ΔLST is significantly negatively correlated to the in situ measured SM ($r = -0.68$, p-value < 0.01). Thus, ΔLST can be used to represent the spatial distribution of SM in the Babao River Basin, and the fitted linear function (indicated in Figure 3) was used to derive daily $\theta_{\Delta LST}^{rep}$ (Figure 4a). However, because of atmospheric effects (e.g., clouds and rain), $\theta_{\Delta LST}^{rep}$ was often missing, as shown in Figure 4a. Indeed, for the study period, atmospheric effects resulted in a high rate of missing ΔLST data (88.6%), especially over the regions with high elevations (Figure 2).

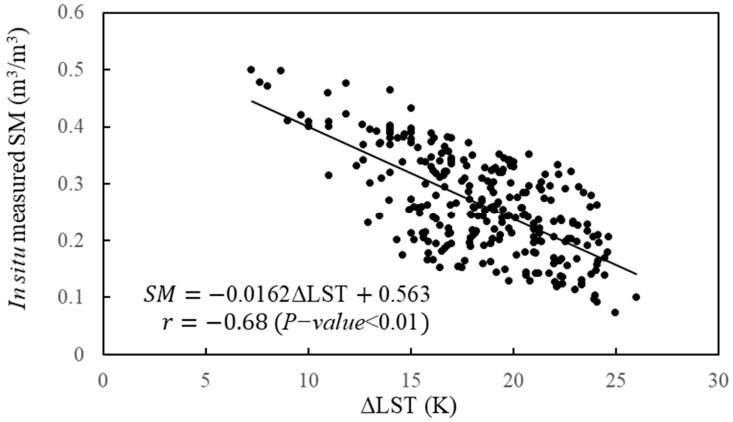

Figure 3. Relationship between the MODIS-derived ΔLST and the in situ measured soil moisture (SM).

To replace the missing $\theta^{rep}_{\Delta LST}$ data, the representative SM (θ^{rep}_{topo}) (Figure 4b) was derived using the combination between topographic factors (elevation and aspect) and the in situ measured SM. Compared with $\theta^{rep}_{\Delta LST}$ (Figure 4a), θ^{rep}_{topo} (Figure 4b) provided a continuous spatial distribution of SM, albeit with less spatial heterogeneity information of SM because the spatial distribution of θ^{rep}_{topo} was reduced to only four regions ($\theta_{high-altitude,\ sunny}$, $\theta_{low-altitude,\ sunny}$, $\theta_{high-altitude,\ shady}$, $\theta_{low-altitude,\ shady}$).

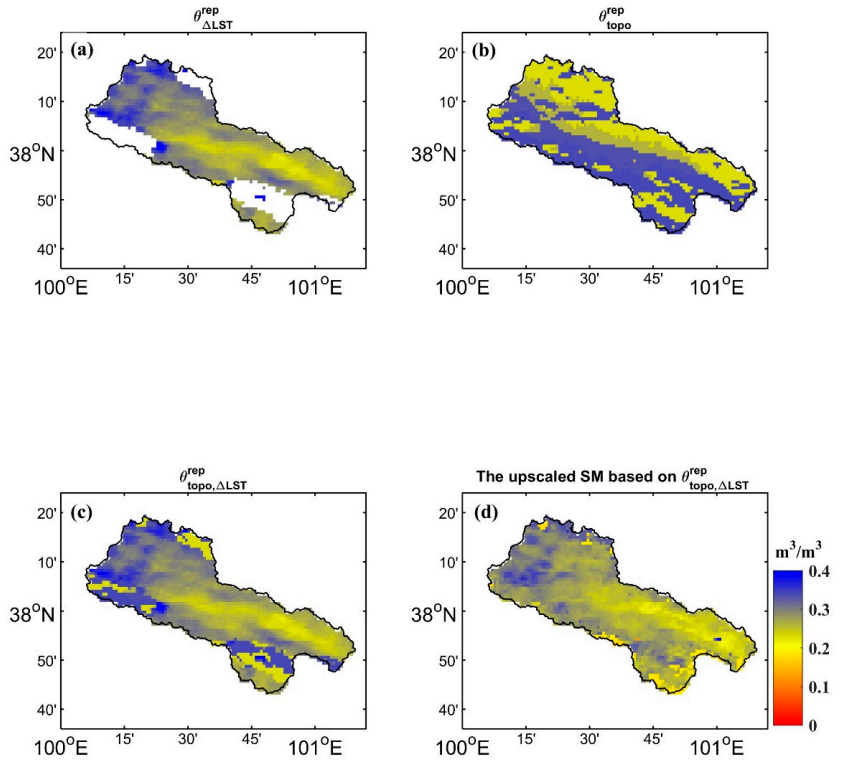

Figure 4. Spatial distribution of representative soil moisture and the upscaled soil moisture on 14 August 2015 in the Babao River Basin. Representative soil moisture (at a spatial resolution of 1 km) derived by ΔLST ($\theta^{rep}_{\Delta LST}$), topography data ($\theta^{rep}_{topo}$), and the combined ΔLST and topography data ($\theta^{rep}_{\Delta LST,\ topo}$) are shown in (**a**–**c**), respectively. The upscaled SM estimates using $\theta^{rep}_{\Delta LST,\ topo}$ are shown in (**d**).

We found that θ^{rep}_{topo} could capture the general temporal dynamics of SM, as observed from the SM dynamics of the four regions (Figure 5); SM in the regions with sunny slopes (the overall average values of $\theta_{high-altitude,\ sunny}$ and $\theta_{low-altitude,\ sunny}$ are 0.21 and 0.23 m^3/m^3, respectively) were lower than in

regions with shady slopes (the overall average values of $\theta_{high-altitude,\ shady}$ and $\theta_{low-altitude,\ shady}$ are 0.31 and 0.33 m^3/m^3, respectively). The temporal variability of SM was also indicated by the different SM conditions between the high-altitude ($\theta_{high-altitude,\ sunny}$ and $\theta_{high-altitude,\ shady}$) and low-altitude regions ($\theta_{low-altitude,\ sunny}$ and $\theta_{low-altitude,\ shady}$). In the sunny slopes, high-altitude regions were generally dryer than low-altitude regions during most of the study period. By contrast, in the shady slopes, the dryer high-altitude regions relative to the low-altitude regions can be observed only after the rainy season, while the SM values in high-altitude regions were similar to those in the low-altitude regions during the rainy season.

Figure 4c shows the spatial distribution of $\theta^{rep}_{topo,\ \Delta LST}$ obtained by combining $\theta^{rep}_{\Delta LST}$ and θ^{rep}_{topo}. It can be seen that $\theta^{rep}_{topo,\ \Delta LST}$ is able to provide a detailed SM pattern over the whole study region. Especially over the regions where $\theta^{rep}_{\Delta LST}$ is missing, $\theta^{rep}_{topo,\ \Delta LST}$ can provide more information on the spatial characteristics and spatio-temporal distribution of SM, compared with $\theta^{rep}_{\Delta LST}$ (Figure 4a). Daily SM at high spatial resolution (1 km) was derived using the BLR upscaling method based on $\theta^{rep}_{topo,\ \Delta LST}$. The upscaled SM (Figure 4d) provided not only a continuous spatial distribution of SM, but also more detailed spatial characteristics of SM, compared with representative SM (Figure 4a–c).

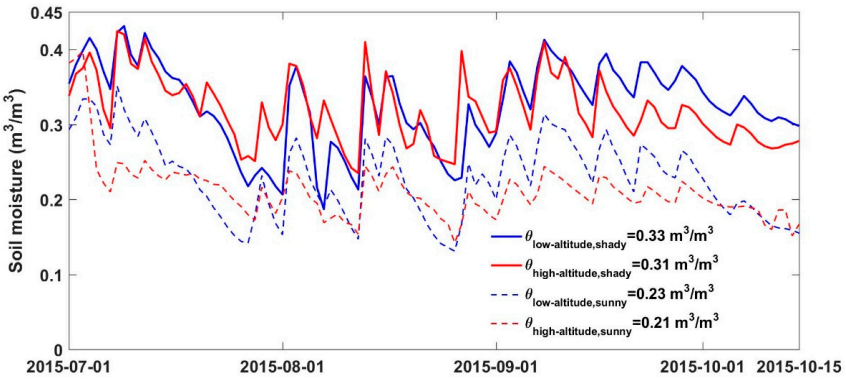

Figure 5. The time-series of the representative soil moisture (θ^{rep}_{topo}) in the regions with high altitude and sunny slope ($\theta_{high-altitude,\ sunny}$), with low altitude and sunny slope ($\theta_{low-altitude,\ sunny}$), with high altitude and shady slope ($\theta_{high-altitude,\ shady}$), and with low altitude and shady slope ($\theta_{low-altitude,\ shady}$), respectively.

4.2. The BLR Performance Evaluation

We quantitatively evaluated the accuracy of the upscaled SM estimates by comparing them against in situ measurements using the leave-one-out cross validation method (Figure 6). Additionally, the two upscaled SM estimates based on $\theta^{rep}_{\Delta LST}$ and $\theta^{rep}_{topo,\ \Delta LST}$ were evaluated to identify whether the upscaling algorithm considering topographic effects ($\theta^{rep}_{topo,\ \Delta LST}$) could increase the accuracy of the SM estimates. The correlation coefficients (r) obtained for the two estimates were similar and generally high (a median r value of 0.80 and 0.82 was obtained for all stations for the SM estimates based on $\theta^{rep}_{\Delta LST}$ and $\theta^{rep}_{topo,\ \Delta LST}$, respectively), except WSN-35 (r = 0.53 and 0.47) and WSN-42 site (r = 0.57 and 0.50, respectively). However, the SM estimates based on $\theta^{rep}_{topo,\ \Delta LST}$ had slope values closer to the one for all stations (ranging from 0.17 to 1.31, with a median value of 0.61), relative to the estimates based on $\theta^{rep}_{\Delta LST}$ (in the range of 0.07 to 0.76, with a median value of 0.31). Also, the SM estimates based on $\theta^{rep}_{topo,\ \Delta LST}$ had higher standard deviation values for all stations (with a median value of 0.029 m^3/m^3), relative to the estimates based on $\theta^{rep}_{\Delta LST}$ (with a median value of 0.015 m^3/m^3). Moreover, the overall ubRMSD values of the estimates based on $\theta^{rep}_{topo,\ \Delta LST}$ (ubRMSD = 0.025 (m^3/m^3)) are lower than that based on $\theta^{rep}_{\Delta LST}$ (ubRMSD = 0.033 (m^3/m^3)). These statistical metrics indicate that the upscaling approach based on $\theta^{rep}_{topo,\ \Delta LST}$ provides more accurate estimates of SM, compared with the ones based on $\theta^{rep}_{\Delta LST}$.

The better performance of the upscaling approach based on $\theta^{rep}_{topo,\ \Delta LST}$ in comparison with that based on $\theta^{rep}_{\Delta LST}$ is also indicated by comparing the two SM estimates against the AMS measurements (Figure 7). The ubRMSD values associated with the SM estimates and the AMS observations were calculated by removing the mean values of the time series. In the comparison between the estimates based on $\theta^{rep}_{\Delta LST}$ and $\theta^{rep}_{topo,\ \Delta LST}$ at the A'rou superstation (Figure 7a), the ubRMSD value decreased from 0.074 to 0.039 m^3/m^3, while the correlation coefficient (slope) increased from 0.23 (0.055) to 0.93 (0.55). The better performance of the upscaling approach based on $\theta^{rep}_{topo,\ \Delta LST}$ was also found at the A'rou sunny AMS station (Figure 7b), providing higher r and slope values and lower ubRMSD values, relative to the estimates based on $\theta^{rep}_{\Delta LST}$. Moreover, better agreements can be seen between the temporal dynamics of the AMS measurements and the estimates based on $\theta^{rep}_{topo,\ \Delta LST}$, compared with the ones based on $\theta^{rep}_{\Delta LST}$ at both AMS stations (Figure 7). Overall, our results suggest that the performance of the upscaling method is successfully improved by including additional SM information associated with topographic effects.

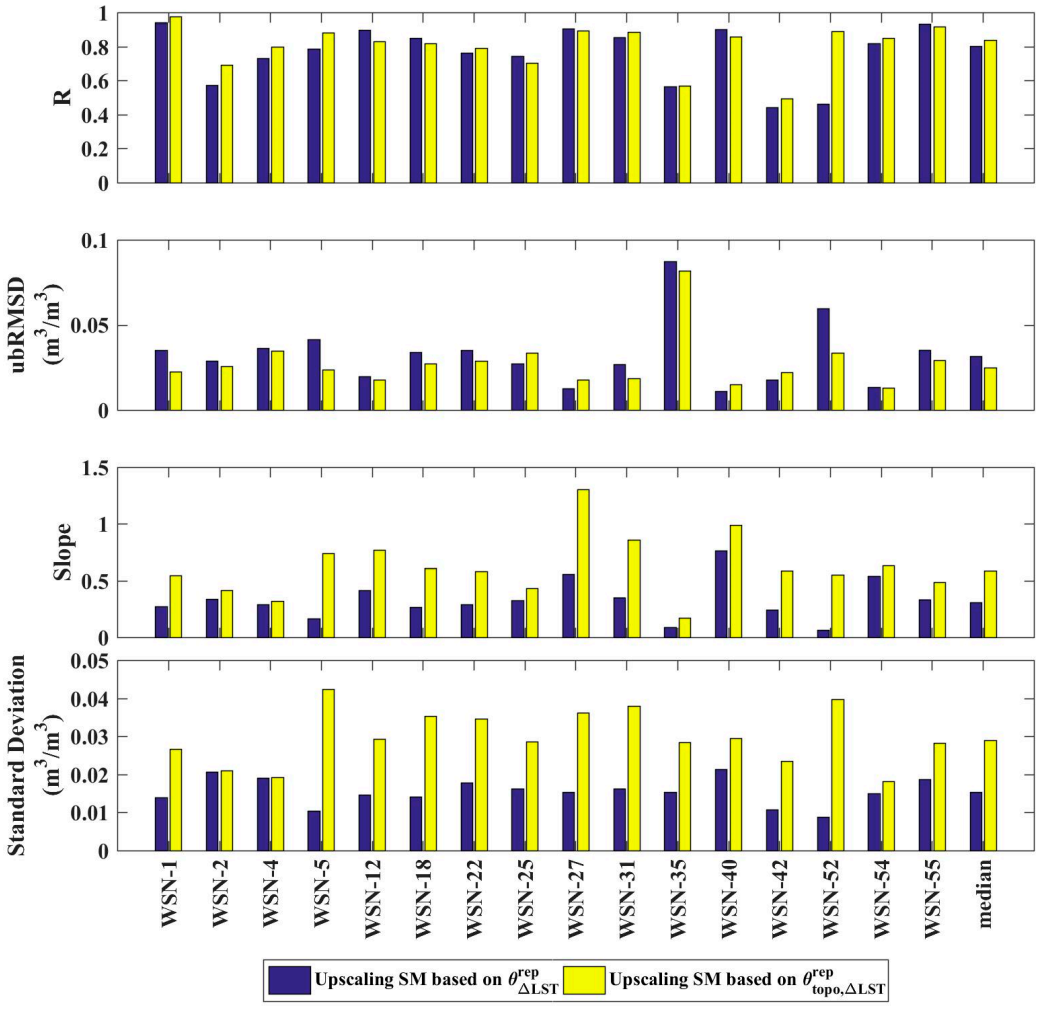

Figure 6. Statistical metrics of the upscaled SM values based on $\theta^{rep}_{\Delta LST}$ and $\theta^{rep}_{topo,\ \Delta LST}$ against the in situ measurements of SM. Note that the median values of each statistical metric are given on the far right of the plot. Slope values were computed between the estimates and the corresponding in situ data using Equation (8). ubRMSD—unbiased root mean square difference.

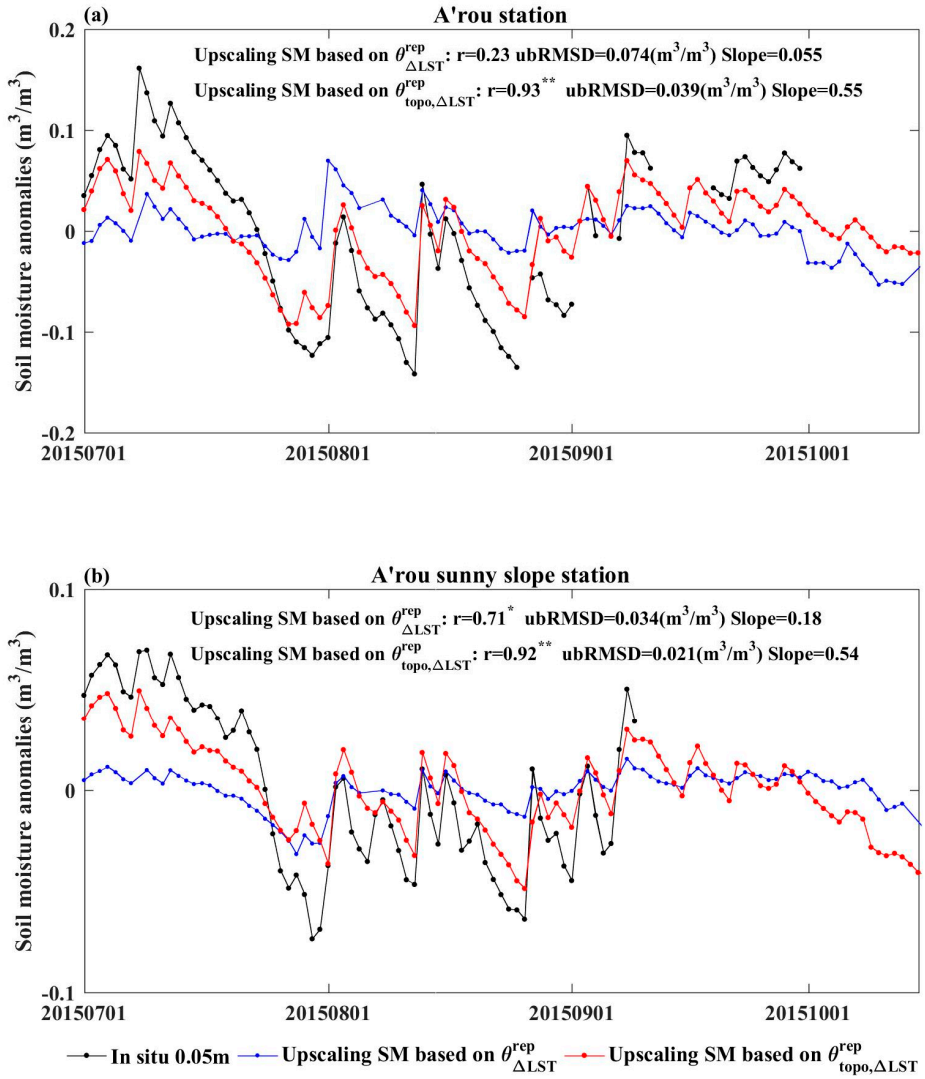

Figure 7. Time series of the upscaled SM based on $\theta^{rep}_{\Delta LST}$ and $\theta^{rep}_{topo,\ \Delta LST}$ against the in situ measured SM at the A'rou superstation (**a**) and the A'rou sunny (**b**) automatic meteorological stations. The ubRMSD values associated with the SM estimates and AMS observations were calculated by removing the mean values of the time series.

5. Discussion

The approach presented in this study was developed to improve SM estimates over mountainous regions by integrating WSN measurements, optical remote sensing data (ΔLST), and topography data (e.g., elevation and aspect). The proposed upscaling method produced satisfactory SM estimates over the mountainous regions. We also found that the SM estimates obtained using the combined SM information ($\theta^{rep}_{topo,\ \Delta LST}$) from topography data and ΔLST provided higher accuracy of SM estimates indicated by better statistical metrics (in particular, slope values were closer to one), compared with the upscaled results using only ΔLST-derived SM information ($\theta^{rep}_{\Delta LST}$). The reason for the better performance of the upscaled approach using $\theta^{rep}_{topo,\ \Delta LST}$ could be partly attributed to the fact that $\theta^{rep}_{topo,\ \Delta LST}$ provides more information on the temporal dynamics of SM, compared with the discontinuous time-series information provided by $\theta^{rep}_{\Delta LST}$. Our approach could address the shortcoming of previous BLR upscaling approaches [25,28] in which the accuracy of the SM estimates is limited by the discontinuity of SM information provided by optical remote sensing data. Moreover, the upscaled

results using $\theta^{rep}_{topo,\ \Delta LST}$ showed a strong ability to capture the extreme values of SM, overcoming the weakness of optical remote sensing data, which are insensitive to extremely dry or wet conditions [22].

However, the approach presented here does not account for the impact of topography on the retrieval of LST over the mountainous terrain. Indeed, over hilly areas, the signature of the surface water status represented by LST could be masked by topographic effects, namely the pixel-scale impact of illumination (solar radiation) and elevation (air temperature) on LST [44,45]. The LST differences between south-facing and north-facing slopes can reach up to 30 °C [46]. LST in high terrain elevation is often lower than for low terrain elevation within the same surface soil water condition, because of the decrease in the air temperature from low to high elevation [44]. These topographic effects limit the application of the widely used surface temperature/vegetation indices (e.g., TVDI and SEE) for the retrieval of high-resolution SM over mountainous regions [4,10], because these indices are derived from the spatial pattern of LST and vegetation indices [47,48]. Conversely, it is likely the topographic effects on LST are mostly removed in the calculation of ΔLST, because the daily difference between day and night LST caused by topographic effects can be negligible. In addition, when dense vegetation covers the soil, LST mostly reflects the status of vegetation, and thus the ability of ΔLST and ATI to capture the SM dynamics becomes weak [49]. Therefore, uncertainties in our proposed upscaling method could be higher in high-density vegetation regions than in low-density vegetation regions; note that most of the study region is covered by the low-density vegetation.

Our results also indicated that θ^{rep}_{topo} could well represent the spatial viability in SM—the SM values in shady (south) slope were higher than those on the sunny (north) slope (Figure 5), which is in line with previous findings [25,50]. This can be explained by the fact that the shady slopes of the Babao River Basin endure frequent rainfalls in summer because of the windward slope location and low evaporation, which results in higher SM than that in the sunny slope regions. After the rainy season, the average SM in the Babao River Basin decreased, with a more rapid decrease on both sunny and shady slopes [25]. Note that the retrieval of θ^{rep}_{topo} assumes that the spatial heterogeneity of SM is mainly influenced by elevation and aspect. Indeed, soil texture and structure and land cover patterns also play an important role in the SM spatial variability [23]. We assumed soil texture and structure and topography to be temporally stable because of the short study period (from July to the middle of October). Indeed, these factors are generally difficult to isolate and measure, and the impact of these factors on the SM variability could vary significantly over time and space. These factors could result in the failure of θ^{rep}_{topo} to represent the spatial viability in SM, which could be one reason explaining why the correlation between the in situ measurements and the estimates using $\theta^{rep}_{topo,\ \Delta LST}$ failed to be improved over WSN-12, 18, 22, 25, 27, 40, and 54 sites, compared with the estimates using $\theta^{rep}_{\Delta LST}$.

It should be noted that the performance of our upscaling method depends not only on the accuracy of representative SM mentioned above, but also on the spatial representativeness of the point-scale in situ measurements. We assumed that the SM distribution within each 1 km grid was homogenous. Indeed, the strong heterogeneities of SM at sub-kilometer-scale could lead to a low representativeness of the ground measurements. Also, this scale mismatch between pixel and point measurements could provide biased estimates. This could be another reason for the poor performance of the SM estimates at WSN-35 and WSN-52 sites, indicated by the low correlation and slope values and high ubRMSD values. Additionally, the grid-scale SM estimates have less variations compared with the ground measurements, because the estimates represent the averaged SM at the grid-scale. This could partly explain why the extreme high SM observations consistently over-predicted the upscaled results and the extreme low SM observations consistently under-predicted the upscaled results (Figure 7).

6. Conclusions

Previous upscaling SM methods were limited by the uncertainties in the estimation caused by the missing observation of optical remote sensing data, especially in mountainous areas with complex terrain. To overcome the estimation uncertainties, we proposed using the combined SM information from optical remote sensing data, topography, and ground measurements. Remote sensing LST and

topographic factors were used as auxiliary information and transformed into a representative SM data-set to capture temporal SM changes at pixel-scale. The BLR method is used to construct the relationship between the multipoint observations and the pixel-scale SM. The proposed method shows the stronger ability to estimate SM dynamics, compared with the method only using optical data. Thus, our study proposed an improved upscaling method to estimate high-resolution SM. The upscaled SM estimates at 1 km with a daily resolution exhibited high estimation accuracy with overall ubRMSD, R, and slope values of 0.025 m^3/m^3, 0.82, and 0.61, respectively. The upscaled SM estimates will be useful for agriculture application for Babao River basin.

It is worth noting that the proposed method could be limited by the representativeness of the in situ measurements and the accuracy of representative SM over other regions. These limitations could be improved in future research by optimizing the sampling method of ground measurements to include more auxiliary data (e.g., land cover patterns and rainfall data) in addition to the topographic effects. Also, further research is needed to develop topography-normalized LST products by correcting the illumination and elevation effects [30] to improve the accuracy of the representative SM over mountainous regions, which may eventually improve the upscaled SM estimates.

Author Contributions: L.F. designed the study. L.F., J.K., R.J., Q.X., and J.W. prepared the in situ measurements. The results were interpreted by L.F., A.A.-Y., J.-P.W., F.F., and J.W. The manuscript was drafted by L.F., A.A.-Y., J.-P.W., F.F., and J.W. with contributions by all co-authors.

Funding: This work was supported by the National Natural Science Foundation of China (Grant No. 41801247), Natural Science Foundation of Jiangsu Province (Grant No. BK20180806), Open Fund of State Key Laboratory of Remote Sensing Science (Grant No. OFSLRSS201801), and National Natural Science Foundation of China (Grant No. 41830648).

Acknowledgments: The authors would like to thank all the scientists, engineers, and students who participated in the HiWATER campaigns, which provided ground data for this work.

Conflicts of Interest: The authors declare no conflict of interest.

References

1. Wigneron, J.-P.; Jackson, T.; O'neill, P.; De Lannoy, G.; De Rosnay, P.; Walker, J.; Ferrazzoli, P.; Mironov, V.; Bircher, S.; Grant, J. Modelling the passive microwave signature from land surfaces: A review of recent results and application to the L-band SMOS & SMAP soil moisture retrieval algorithms. *Remote Sens. Environ.* **2017**, *192*, 238–262.
2. Fan, L.; Wigneron, J.-P.; Xiao, Q.; Al-Yaari, A.; Wen, J.; Martin-StPaul, N.; Dupuy, J.-L.; Pimont, F.; Al Bitar, A.; Fernandez-Moran, R. Evaluation of microwave remote sensing for monitoring live fuel moisture content in the Mediterranean region. *Remote Sens. Environ.* **2018**, *205*, 210–223. [CrossRef]
3. Al-Yaari, A.; Wigneron, J.-P.; Ducharne, A.; Kerr, Y.; De Rosnay, P.; De Jeu, R.; Govind, A.; Al Bitar, A.; Albergel, C.; Munoz-Sabater, J. Global-scale evaluation of two satellite-based passive microwave soil moisture datasets (SMOS and AMSR-E) with respect to Land Data Assimilation System estimates. *Remote Sens. Environ.* **2014**, *149*, 181–195. [CrossRef]
4. Merlin, O.; Walker, J.P.; Chehbouni, A.; Kerr, Y. Towards deterministic downscaling of SMOS soil moisture using MODIS derived soil evaporative efficiency. *Remote Sens. Environ.* **2008**, *112*, 3935–3946. [CrossRef]
5. Peng, J.; Shen, H.; Wu, J.S. Soil moisture retrieving using hyperspectral data with the application of wavelet analysis. *Environ. Earth Sci.* **2013**, *69*, 279–288. [CrossRef]
6. Kerr, Y.H.; Al-Yaari, A.; Rodriguez-Fernandez, N.; Parrens, M.; Molero, B.; Leroux, D.; Bircher, S.; Mahmoodi, A.; Mialon, A.; Richaume, P. Overview of SMOS performance in terms of global soil moisture monitoring after six years in operation. *Remote Sens. Environ.* **2016**, *180*, 40–63. [CrossRef]
7. Njoku, E.G.; Jackson, T.J.; Lakshmi, V.; Chan, T.K.; Nghiem, S.V. Soil moisture retrieval from AMSR-E. *IEEE Trans. Geosci. Remote Sens.* **2003**, *41*, 215–229. [CrossRef]
8. Entekhabi, D.; Njoku, E.G.; O'Neill, P.E.; Kellogg, K.H.; Crow, W.T.; Edelstein, W.N.; Entin, J.K.; Goodman, S.D.; Jackson, T.J.; Johnson, J. The soil moisture active passive (SMAP) mission. *Proc. IEEE* **2010**, *98*, 704–716. [CrossRef]

9. Das, N.N.; Entekhabi, D.; Njoku, E.G. An algorithm for merging SMAP radiometer and radar data for high-resolution soil-moisture retrieval. *IEEE Trans. Geosci. Remote Sens.* **2011**, *49*, 1504–1512. [CrossRef]
10. Merlin, O.; Rudiger, C.; Al Bitar, A.; Richaume, P.; Walker, J.P.; Kerr, Y.H. Disaggregation of SMOS soil moisture in Southeastern Australia. *IEEE Trans. Geosci. Remote Sens.* **2012**, *50*, 1556–1571. [CrossRef]
11. Piles, M.; Sánchez, N.; Vall-llossera, M.; Camps, A.; Martínez-Fernández, J.; Martínez, J.; González-Gambau, V. A downscaling approach for SMOS land observations: Evaluation of high-resolution soil moisture maps over the Iberian Peninsula. *IEEE J. Sel. Top. Appl. Earth Obs. Remote Sens.* **2014**, *7*, 3845–3857. [CrossRef]
12. Chauhan, N.; Miller, S.; Ardanuy, P. Spaceborne soil moisture estimation at high resolution: A microwave-optical/IR synergistic approach. *Int. J. Remote Sens.* **2003**, *24*, 4599–4622. [CrossRef]
13. Peng, J.; Loew, A.; Merlin, O.; Verhoest, N.E. A review of spatial downscaling of satellite remotely sensed soil moisture. *Rev. Geophys.* **2017**, *55*, 341–366. [CrossRef]
14. Kerr, Y.H.; Waldteufel, P.; Wigneron, J.-P.; Martinuzzi, J.; Font, J.; Berger, M. Soil moisture retrieval from space: The Soil Moisture and Ocean Salinity (SMOS) mission. *IEEE Trans. Geosci. Remote Sens.* **2001**, *39*, 1729–1735. [CrossRef]
15. Qiu, Y.; Fu, B.; Wang, J.; Chen, L. Spatial variability of soil moisture content and its relation to environmental indices in a semi-arid gully catchment of the Loess Plateau, China. *J. Arid Environ.* **2001**, *49*, 723–750. [CrossRef]
16. Bárdossy, A.; Lehmann, W. Spatial distribution of soil moisture in a small catchment. Part 1: Geostatistical analysis. *J. Hydrol.* **1998**, *206*, 1–15. [CrossRef]
17. Anderson, S.P.; Bales, R.C.; Duffy, C.J. Critical Zone Observatories: Building a network to advance interdisciplinary study of Earth surface processes. *Mineral. Mag.* **2008**, *72*, 7–10. [CrossRef]
18. Li, X.; Cheng, G.; Liu, S.; Xiao, Q.; Ma, M.; Jin, R.; Che, T.; Liu, Q.; Wang, W.; Qi, Y. Heihe watershed allied telemetry experimental research (HiWATER): Scientific objectives and experimental design. *Bull. Am. Meteorol. Soc.* **2013**, *94*, 1145–1160. [CrossRef]
19. Greifeneder, F.; Notarnicola, C.; Bertoldi, G.; Niedrist, G.; Wagner, W. From point to pixel scale: An upscaling approach for in situ soil moisture measurements. *Vadose Zone J.* **2016**, *15*. [CrossRef]
20. Kang, J.; Jin, R.; Li, X. Regression kriging-based upscaling of soil moisture measurements from a wireless sensor network and multiresource remote sensing information over heterogeneous cropland. *IEEE Geosci. Remote Sens. Lett.* **2015**, *12*, 92–96. [CrossRef]
21. Gao, S.; Zhu, Z.; Liu, S.; Jin, R.; Yang, G.; Tan, L. Estimating the spatial distribution of soil moisture based on Bayesian maximum entropy method with auxiliary data from remote sensing. *Int. J. Appl. Earth Obs. Geoinform.* **2014**, *32*, 54–66. [CrossRef]
22. Fan, L.; Xiao, Q.; Wen, J.; Liu, Q.; Jin, R.; You, D.; Li, X. Mapping high-resolution soil moisture over heterogeneous cropland using multi-resource remote sensing and ground observations. *Remote Sens.* **2015**, *7*, 13273–13297. [CrossRef]
23. Crow, W.T.; Berg, A.A.; Cosh, M.H.; Loew, A.; Mohanty, B.P.; Panciera, R.; de Rosnay, P.; Ryu, D.; Walker, J.P. Upscaling sparse ground-based soil moisture observations for the validation of coarse-resolution satellite soil moisture products. *Rev. Geophys.* **2012**, *50*. [CrossRef]
24. Fan, L.; Xiao, Q.; Wen, J.; Liu, Q.; Tang, Y.; You, D.; Wang, H.; Gong, Z.; Li, X. Evaluation of the airborne CASI/TASI Ts-VI space method for estimating near-surface soil moisture. *Remote Sens.* **2015**, *7*, 3114–3137. [CrossRef]
25. Kang, J.; Jin, R.; Li, X.; Ma, C.; Qin, J.; Zhang, Y. High spatio-temporal resolution mapping of soil moisture by integrating wireless sensor network observations and MODIS apparent thermal inertia in the Babao River Basin, China. *Remote Sens. Environ.* **2017**, *191*, 232–245. [CrossRef]
26. Djamai, N.; Magagi, R.; Goïta, K.; Merlin, O.; Kerr, Y.; Roy, A. A combination of DISPATCH downscaling algorithm with CLASS land surface scheme for soil moisture estimation at fine scale during cloudy days. *Remote Sens. Environ.* **2016**, *184*, 1–14. [CrossRef]
27. Chen, T.; Martin, E. Bayesian linear regression and variable selection for spectroscopic calibration. *Anal. Chim. Acta* **2009**, *631*, 13–21. [CrossRef]
28. Qin, J.; Yang, K.; Lu, N.; Chen, Y.; Zhao, L.; Han, M. Spatial upscaling of in-situ soil moisture measurements based on MODIS-derived apparent thermal inertia. *Remote Sens. Environ.* **2013**, *138*, 1–9. [CrossRef]

29. Hassan, Q.K.; Bourque, C.P.-A.; Meng, F.-R.; Cox, R.M. A wetness index using terrain-corrected surface temperature and normalized difference vegetation index derived from standard MODIS products: An evaluation of its use in a humid forest-dominated region of eastern Canada. *Sensors* **2007**, *7*, 2028–2048. [CrossRef]
30. Cherubini, F.; Vezhapparambu, S.; Bogren, W.; Astrup, R.; Strømman, A.H. Spatial, seasonal, and topographical patterns of surface albedo in Norwegian forests and cropland. *Int. J. Remote Sens.* **2017**, *38*, 4565–4586. [CrossRef]
31. Li, X.; Li, X.; Li, Z.; Ma, M.; Wang, J.; Xiao, Q.; Liu, Q.; Che, T.; Chen, E.; Yan, G. Watershed allied telemetry experimental research. *J. Geophys. Res. Atmos.* **2009**, *114*. [CrossRef]
32. Yong, G.; Jianghao, W.; Jinfeng, W.; Rui, J.; Maogui, H. Regression Kriging model-based sampling optimization design for the eco-hydrology wireless sensor network. *Adv. Earth Sci.* **2012**, *27*, 1006–1013.
33. Kang, J.; Tan, J.; Jin, R.; Li, X.; Zhang, Y. Reconstruction of MODIS land surface temperature products based on multi-temporal information. *Remote Sens.* **2018**, *10*, 1112. [CrossRef]
34. Jin, R.; Li, X.; Liu, S. Understanding the heterogeneity of soil moisture and evapotranspiration using multiscale observations from satellites, airborne sensors, and a ground-based observation matrix. *IEEE Geosci. Remote Sens. Lett.* **2017**, *14*, 2132–2136. [CrossRef]
35. Liu, S.; Li, X.; Xu, Z.; Che, T.; Xiao, Q.; Ma, M.; Liu, Q.; Jin, R.; Guo, J.; Wang, L. The Heihe Integrated Observatory Network: A Basin-Scale Land Surface Processes Observatory in China. *Vadose Zone J.* **2018**, *17*. [CrossRef]
36. Wan, Z.; Zhang, Y.; Zhang, Q.; Li, Z.-L. Quality assessment and validation of the MODIS global land surface temperature. *Int. J. Remote Sens.* **2004**, *25*, 261–274. [CrossRef]
37. Westermann, S.; Langer, M.; Boike, J. Spatial and temporal variations of summer surface temperatures of high-arctic tundra on Svalbard—implications for MODIS LST based permafrost monitoring. *Remote Sens. Environ.* **2011**, *115*, 908–922. [CrossRef]
38. Tachikawa, T.; Hato, M.; Kaku, M.; Iwasaki, A. Characteristics of ASTER GDEM version 2. In Proceedings of the 2011 IEEE International Geoscience and Remote Sensing Symposium (IGARSS), Vancouver, BC, Canada, 24–29 July 2011; pp. 3657–3660.
39. Zhong, B.; Yang, A.; Nie, A.; Yao, Y.; Zhang, H.; Wu, S.; Liu, Q. Finer resolution land-cover mapping using multiple classifiers and multisource remotely sensed data in the Heihe River Basin. *IEEE J. Sel. Top. Appl. Earth Obs. Remote Sens.* **2015**, *8*, 4973–4992. [CrossRef]
40. Cawley, G.C.; Talbot, N.L. Efficient leave-one-out cross-validation of kernel fisher discriminant classifiers. *Pattern Recognit.* **2003**, *36*, 2585–2592. [CrossRef]
41. Al-Yaari, A.; Wigneron, J.-P.; Dorigo, W.; Colliander, A.; Pellarin, T.; Hahn, S.; Mialon, A.; Richaume, P.; Fernandez-Moran, R.; Fan, L. Assessment and inter-comparison of recently developed/reprocessed microwave satellite soil moisture products using ISMN ground-based measurements. *Remote Sens. Environ.* **2019**, *224*, 289–303. [CrossRef]
42. Al-Yaari, A.; Wigneron, J.-P.; Kerr, Y.; Rodriguez-Fernandez, N.; O'Neill, P.; Jackson, T.; De Lannoy, G.; Al Bitar, A.; Mialon, A.; Richaume, P. Evaluating soil moisture retrievals from ESA's SMOS and NASA's SMAP brightness temperature datasets. *Remote Sens. Environ.* **2017**, *193*, 257–273. [CrossRef]
43. Entekhabi, D.; Reichle, R.H.; Koster, R.D.; Crow, W.T. Performance metrics for soil moisture retrievals and application requirements. *J. Hydrometeorol.* **2010**, *11*, 832–840. [CrossRef]
44. Malbéteau, Y.; Merlin, O.; Gascoin, S.; Gastellu, J.-P.; Mattar, C.; Olivera-Guerra, L.; Khabba, S.; Jarlan, L. Normalizing land surface temperature data for elevation and illumination effects in mountainous areas: A case study using ASTER data over a steep-sided valley in Morocco. *Remote Sens. Environ.* **2017**, *189*, 25–39. [CrossRef]
45. Ermida, S.L.; DaCamara, C.C.; Trigo, I.F.; Pires, A.C.; Ghent, D.; Remedios, J. Modelling directional effects on remotely sensed land surface temperature. *Remote Sens. Environ.* **2017**, *190*, 56–69. [CrossRef]
46. Raz-Yaseef, N.; Rotenberg, E.; Yakir, D. Effects of spatial variations in soil evaporation caused by tree shading on water flux partitioning in a semi-arid pine forest. *Agric. For. Meteorol.* **2010**, *150*, 454–462. [CrossRef]
47. Sandholt, I.; Rasmussen, K.; Andersen, J. A simple interpretation of the surface temperature/vegetation index space for assessment of surface moisture status. *Remote Sens. Environ.* **2002**, *79*, 213–224. [CrossRef]
48. Carlson, T. An overview of the" triangle method" for estimating surface evapotranspiration and soil moisture from satellite imagery. *Sensors* **2007**, *7*, 1612–1629. [CrossRef]

49. Sobrino, J.; Franch, B.; Mattar, C.; Jiménez-Muñoz, J.; Corbari, C. A method to estimate soil moisture from Airborne Hyperspectral Scanner (AHS) and ASTER data: Application to SEN2FLEX and SEN3EXP campaigns. *Remote Sens. Environ.* **2012**, *117*, 415–428. [CrossRef]
50. Ge, Y.; Wang, J.; Heuvelink, G.B.; Jin, R.; Li, X.; Wang, J. Sampling design optimization of a wireless sensor network for monitoring ecohydrological processes in the Babao River basin, China. *Int. J. Geogr. Inf. Sci.* **2015**, *29*, 92–110. [CrossRef]